

Research Paper

Photodynamic therapy at ultra-low NIR laser power and X-Ray imaging using Cu_3BiS_3 nanocrystals

Srivani Veerananarayanan^{1*}, M. Sheikh Mohamed^{1,2*}, Aby Cheruvathoor Poulouse^{1*}, Masuko Rinya³, Yasushi Sakamoto⁴, Toru Maekawa^{1,2}, D. Sakthi Kumar^{1,2} 

1. Bio-Nano Electronics Research Centre, Toyo University, Kawagoe, 350-8585, Japan
2. Graduate School of Interdisciplinary New Science, Toyo University, Kawagoe, 350-8585, Japan
3. JEOL Ltd. Otemachi Nomura Bldg.13F, 2-1-1, Otemachi, Chiyoda, Tokyo, 100-0004, Japan
4. Biomedical Research Centre, Division of Analytical Science, Saitama Medical University, Saitama 350-0495, Japan

* Equal contributing Authors

 Corresponding author: Prof. D. Sakthi Kumar, Ph: 81-492-39-1636 Fax: 81-492-34-2502 E-mail: sakthi@toyo.jp

© Ivyspring International Publisher. This is an open access article distributed under the terms of the Creative Commons Attribution (CC BY-NC) license (<https://creativecommons.org/licenses/by-nc/4.0/>). See <http://ivyspring.com/terms> for full terms and conditions.

Received: 2018.02.01; Accepted: 2018.08.19; Published: 2018.10.21

Abstract

Materials with efficient potential in imaging as well as therapy are gaining particular attention in current medical research. Photodynamic therapy (PDT) has been recently recognized as a promising treatment option for solid tumors. Still, most of the nanomaterial-based PDT modules either employ an additional photosensitizer or require high power laser sources. Also, they suffer from a lack of responsiveness in the near-infrared (NIR) region. Nanomaterials that could realize PDT independently (without any photosensitizer), at safe laser dose and in the deep tissue penetrative NIR region would definitely be better solid tumor treatment options.

Methods: Herein, Cu- and Bi-based bimetal chalcogenide (Cu_3BiS_3), with absorption in the NIR region was developed. High-performance PDT of cancer and high-contrast x-ray imaging of tumor were performed *in vivo*. Biocompatibility of the NCs was also assessed *in vivo*.

Results: The highlight of the results was the realization of ultra-low dose NIR laser-mediated PDT, which has not been achieved before, leading to complete tumor regression. This could be a breakthrough in providing a pain- and scar-less treatment option, especially for solid tumors and malignant/benign subcutaneous masses. Though the NCs are active in the photo-thermal therapy (PTT) regime as well, focus is given to the exciting aspect of extremely low power-induced PDT observed here.

Conclusion: Their extended *in vivo* biodistribution with commendable hemo- and histo-compatibilities, along with imaging and multi-therapeutic capabilities, project these Cu_3BiS_3 NCs as promising, prospective theranostic candidates.

Key words: photodynamic therapy, x-ray contrast imaging, reactive oxygen species, near-infrared laser, anticancer therapy

Introduction

Singlet oxygen ($^1\text{O}_2$) is a crucial reactive oxygen species (ROS) involved in clinical photodynamic therapy (PDT) of various cancers [1]. It is considered to be an effective therapeutic modality with advantages of great spatiotemporal selectivity and minimal invasiveness. It has recently been reported that apart from the ROS-mediated killing of cancer

cells, PDT also has the tendency to induce an anti-tumor immune response against the same, thereby acting as a bimodal therapeutic strategy [2]. The major conventional sources for $^1\text{O}_2$ generation are organic photosensitizers such as silicon phthalocyanine, rose bengal, porphyrins, etc. These molecules, though they have been successful to an

extent, still greatly suffer from limitations like enzymatic degradation, photochemical bleaching etc. apart from predominantly being active in the UV and/or visible region [3, 4] with only few responsive in NIR region [5-7]. For PDT of tumors in biological systems, probes responsive to near-infrared (NIR) light are of particular interest, since light of this wavelength range has much deeper penetration than visible light and biological tissues have the least absorption within the 650–900 nm NIR range, signifying the need for NIR light-active PDT photosensitizers [8].

Nanomaterials for bio-applications are gaining momentum due to their advantageous role of performing multiple functions simultaneously [9-13]. Multifunctional nanocrystals (NCs) with simultaneous imaging and therapeutic potential are highly attractive as they can serve for image-guided therapy and be considered for personalized medicine [14-20]. To serve multiple functions with equal efficacy, NCs made up of a unique mix of elements, with each elemental presence defining a set function, are complex to prepare and require a basic understanding of the elements, their combinations, nucleation and formation. Few nanoparticles (NPs) have been observed to sensitize and generate $^1\text{O}_2$ due to localized surface plasmon resonance (LSPR) [21]. However, NPs, especially metal-based, are resistant to enzymatic or photochemical degradation, giving them an edge over their organic counterparts [22, 23]. Also, nanomaterial-based photosensitizers are required in comparatively lower quantities than organic dye sensitizers to produce significant $^1\text{O}_2$ for effective PDT, due to their higher extinction coefficients [24]. To this end, several nanostructures, such as, gold, silver, fullerene, Cu_2S , $\text{W}_{18}\text{O}_{49}$, $\text{Cu}_2(\text{OH})\text{PO}_4$, UCNPs, Cs_xWO_3 , etc. were reported as NIR light-active PDT agents [10, 25-33]. However, NIR-induced PDT is greatly restricted by heating of cells and tissues. This temperature rise results in low yields of ROS, thereby leading to synergistic photothermal-photodynamic effects, where the cell death occurs mostly via photothermal heating [34]. Also, the usage of high laser irradiance (1-48 W/cm^2) is practically not applicable for clinical treatment of tumors, as they exceed the skin tolerance threshold values (maximum permissible exposure (MPE) of skin at 808 nm is 350 mW/cm^2 , with an exposure time of 10-1000 s) set by the American National Standards Institute (ANSI) [35]. Not many NCs are reported to mediate PDT at low laser dosage, along with issues such as localized heating (PTT effect) resulting in highly diminished ROS generation. A few examples of NP-mediated (without photosensitizers) PDT are summarized in **Table S1**, most with laser irradiances

above 100 mW/cm^2 and an average localized temperature rise of 4-12 $^\circ\text{C}$, suggesting the supportive role of heat in the tumoricidal effects. Therefore, it is essential to develop newer PDT-mediating nanomaterials that can utilize low laser doses/photo-energy to kill cancer cells more effectively within the tolerance of skin burning thresholds, thereby facilitating a pain- and scar-less treatment.

The present work describes the facile preparation and application of metal chalcogenide NCs composed of Cu and Bi. Bi, with high x-ray attenuation is proposed to serve as an efficient x-ray contrast probe [36], whereas Cu ions in the NCs, with their broad NIR absorption, serve as NIR-responsive photodynamic and thermal therapy agents [37]. Though few Cu- and Bi-based chalcogenides have been reported [38-43], their ability to induce PDT has not been observed till now, making this the primary report. Apart from being cytocompatible, the theranostic properties of copper bismuth sulfide (Cu_3BiS_3) NCs under *in vitro* and *in vivo* conditions were evaluated. The 808 nm NIR laser-induced generation of ROS under ultra-low laser power (10 mW) was observed, without any instrumentally detectable (IR thermal camera) rise in temperature. The NCs also exhibited strong x-ray attenuation for computed tomography (CT) imaging. Additional PTT experiments were carried out *in vitro* to provide a multi-dimensional approach of the NCs towards cancer killing. Therefore, these Cu_3BiS_3 NCs are presumed to hold great potential in cancer theranostics as well as the biomedical field as a whole. To the best of our knowledge, this is the first reported example of a nanomaterial-mediated PDT with such a low laser power to efficiently exterminate cancer cells *in vitro* and tumors *in vivo*.

Methods

Materials

Dulbecco's modified Eagle's medium (DMEM), phosphate buffered saline (PBS) (pH 7.2), DCFH-DA and live/dead cell double staining kit were purchased from Sigma-Aldrich. 0.25% Trypsin, antibiotics (penicillin and streptomycin) and fetal bovine serum (FBS) were obtained from Gibco. Alamar Blue and Cell ROX were purchased from Invitrogen. DSPE-PEG (2000) amine-(1,2-distearoyl-sn-glycero-3-phosphoethanolamine-N-[amino(polyethylene glycol)-2000] (ammonium salt)) was purchased from Avanti polar lipids. Annexin *in vivo* 750 was acquired from PerkinElmer. All other chemicals and reagents were of analytical grade and acquired from either Sigma-Aldrich or Wako chemicals.

Cu₃BiS₃ NC synthesis and PEGylation

20 mmol of Cu(OAc)₂ was dissolved in 10 mL deionized water under magnetic stirring to which 50 mmol 2,4 pentanedione was added and kept stirring for 20 min. Post 20 min, triethylamine was added to precipitate Cu(acac)₂. The precipitate was washed repeatedly with ethanol and the final product was freeze-dried to obtain a powder. The same procedure was used for the preparation of Bi(acac)₃ from Bi(OAc)₃. Cu₃BiS₃ NCs were prepared by a hot injection method using organic solvents. 3 mmol of Cu(acac)₂ and 1 mmol of Bi(acac)₃ powder were dissolved in 10 mL of oleic acid with 2 mL of oleylamine by stirring at 150 °C under vacuum for 30 min. Sulfur precursor was prepared using 3 mmol of sulfur dissolved in 5 mL of octadecene under vigorous stirring and heating at 150 °C, which yielded a transparent solution. 5 mL of sulfur precursor solution was quickly injected into copper precursor solution and the reaction was carried out at 200 °C for 30 min under Ar atmosphere. The reaction was quenched in a cold bath and the NCs were precipitated with ethanol thrice and centrifuged; the obtained precipitate was re-dispersed in chloroform. The lipid-PEGylation of NCs was performed using a thin-film hydration method. Typically, DSPE-PEG-amine dissolved in chloroform (5 mg/mL) was added to 1 mg/mL of the NCs suspended in chloroform. The solution was gently evaporated to obtain a thin film of NCs and lipid-PEG. This thin film was then hydrated with PBS buffer and the suspension was sonicated for 15 min. The PEGylated NCs were separated by repeated centrifugation and washing. An aqueous suspension of NCs functionalized with PEG was thus obtained.

Analyses parameters, instrumentation and characterization

The morphology of the as-prepared NCs was analyzed with the help of a field emission transmission electron microscope (TEM; JEOL JEM-2100). The elemental composition of the NCs was analyzed using EDS (JEOL JED-2300T) and the elemental mapping was done using ARM-200F by STEM mode using JEOL EDS. X-ray photoelectron spectroscopy (XPS) measurements were carried out using Kratos, Shimadzu with anode mono Al, a pass energy of 40, current of 10 mA and voltage of 12 kV. The powder x-ray diffraction (XRD) pattern was measured on a Rigaku (RINT) diffractometer equipped with a rotating anode. The 2θ angle for the XRD spectra was recorded at a scanning rate of 5°/min. The zeta potential and average hydrodynamic size of the NCs before and after PEGylation was determined by a Nano-ZS 168

Zetasizer (Malvern Instruments Ltd). To investigate the surface chemical bonding and characteristics of bare and PEGylated NCs, Fourier transform infrared spectroscopy was performed with the help of a Spectrum 100 FT-IR Spectrometer (Perkin Elmer) connected with a Universal ATR Sampling Accessory. The absorption spectrum of the NCs was analyzed using a UV-Vis-NIR spectroscope (JASCO V-570 UV/Vis/NIR spectrophotometer). Photoluminescence spectra of ROS production were recorded with an excitation wavelength of 365 nm using a JASCO FP 750 spectrofluorometer. DCFH-DA assay for ROS production and cell viability assessment was done with a microplate spectrophotometer (multidetector microplate scanner, Dainippon Sumitomo Pharma). High-speed confocal laser-scanning microscopy (CLSM, Olympus IX 81 under DU897 mode) was used to analyze live/dead-stained cell populations and intracellular ROS production. A highly monochromatic, collimated beam of NIR range (800 nm) (Chameleon Ultra Diode-Pumped Mode Locked-Sub Femtosecond Laser, coherent 80 MHz repetition rate) with an irradiance of 1.726 W/cm² (laser power meter: VEGA, OPHIR, Japan) was utilized for all PTT experiments. For PDT experiments, a portable hand-held NIR laser (laser diode, 808 nm, 10 mW, Edmund Optics) was utilized. The temperature variations were measured with an infrared (IR) thermometer (thermal imager T885, Testo AG, Germany). μCT contrast potential was analyzed at 45 keV tube voltage using a μCT system (μCT 35 desktop microCT scanner, Scanco Medical, Switzerland). The annexin *in vivo* live imaging of mice was carried out using a Clairvivo OPT (Shimadzu, Japan) using ICG filters. Cryosectioning of the organs was performed on a Leica CM1900. The histo-sections were imaged using a Keyence BZ-X700 microscope. Cells, organs, excreta and blood were digested using nitric acid in an advanced microwave digestion system (Ethos Easy, Milestone). The atomic percentage of Cu and Bi as well the Cu ion leaching post irradiation were estimated using inductively coupled plasma mass spectrometry (ICP-MS, iCAP Q, Thermofisher Scientific).

Cell culture studies

MCF-7 (human breast adenocarcinoma) and HMEC (human mammary epithelial) cells were acquired from Riken Bioresources, Japan and ATCC respectively, and maintained in T25 flasks (TPP) using DMEM medium supplemented with 10% FBS and antibiotics in an incubator at 37 °C with 5% CO₂. The cells were sub-cultured every 4 days. Cells were cultured on 35 mm glass base dishes (IWAKI) for

confocal microscopy studies and in 96-well plates (IWAKI) for cytotoxicity studies. Cytotoxicity was assayed with the help of alamar blue. The principle of the assay involves the conversion of non-fluorescent alamar blue into a fluorescent moiety, whose absorbance can be read at 560 nm, by metabolically active cells and is not converted by dying cells. Post confluency, MCF-7 and HMEC were trypsinized, pelleted and approximately 5000 cells were added to each well of 96-well plates and cultured for 24 h prior to NPs exposure. All experiments were conducted in triplicates. Controls were maintained devoid of any treatment, whereas test groups were treated with 100 μ L (1 mg/mL, 0.5 mg/mL and 0.1 mg/mL) of respective NCs. The plates were incubated for 48 h after which the fluorescence intensity of the final product was analyzed with a microplate spectrofluorimeter. The viable percentage of cells was calculated for each group and plotted against concentration of NCs. For analysis of cellular internalization of the NCs, cells were plated onto T25 flasks and allowed to grow to visual confluency. 100 μ L of 0.05 mg/mL and 0.25 mg/mL NPs were added to the plates and incubated for 24 h at culture conditions followed by trypsinization and digestion with nitric acid for ICP-MS analysis. To determine the concentration-dependent photothermal responsiveness of NCs, different concentrations of water-dispersed NCs were irradiated with NIR laser of 800 nm with an irradiance of 1.726 W/cm². The heating and cooling profiles were recorded every 30 s and graphed. To further investigate the photothermal conversion efficiency of the NCs, we recorded the temperature change of the sample (100 μ g/mL) as a function of time under NIR laser for 600 s. For photothermal ablation of cells, approximately 25,000 cells were grown in glass base dishes. The cells were treated with NCs (0.1 mg/mL) and subjected to NIR laser exposure for 2 min, after which they were stained using Calcein/PI live/dead staining kit. All the experiments were conducted in triplicates and the cells were thoroughly washed to remove unbound NCs and stains prior to analysis. To analyze the effect of PDT, cells were exposed to (100 μ g/mL) NCs for 4 h, post which, they were washed to remove the unbound NCs. After washing with PBS, the cells were exposed to 808 nm, 10 mW/cm² NIR laser for 10 min. Cell ROX tracer was then added to image the intracellular ROS production with the help of CLSM. Quantitative analysis of ROS was done using DCFH-DA method in a 96-well plate. The confluent cells in 96-well plates were subjected to NC treatment, followed by laser irradiation. The amount of ROS produced was quantified by adding DCFH for 30 min. The emission of DCFH-DA was quantified at 520 nm

and tabulated. For quantitative analysis of cell viability, cells grown in 96-well plates were exposed to NCs for 4 h and then irradiated with low-power NIR laser, 808 nm, 10 mW for 10 min. The cells were then analyzed for viability 4 h post NIR irradiation, using alamar blue assay. For μ CT analysis, MCF-7 cells were treated with 0.25 and 0.5 mg/mL Cu₃BiS₃ NCs for 24 h, thoroughly washed with PBS, centrifuged and the pellet was exposed to x-rays.

In vivo studies

All *in vivo* animal procedures were in compliance with the guidelines of the Institutional Animal Care and Use Committee, Saitama Medical University, Japan (Approval No. 2179). 5-week-old BALB/c nu/nu mice were utilized for the experiments. For *in vivo* biocompatibility analyses, mice were divided into two groups, controls and Cu₃BiS₃ NCs treated. Controls were injected intravenously with saline whereas the treatment group mice were injected with 1 mg (40 mg/kg of body weight) of NCs. The weights of the animals in each group were analyzed before the injection and every 5 days after injection until the endpoint (15 days). For histology analyses, animals were euthanized at 1 and 14 days post injection, and major organs (brain, heart, lungs, liver, spleen and kidney) and blood samples were collected. The major organs were perfused, cryopreserved and sectioned for H&E staining. The stained sections were imaged using a brightfield microscope. The blood samples were processed to collect serum, which were then analyzed for biochemical parameters such as total protein, albumin, adenine/guanine ratio, blood urea nitrogen, creatinine, uric acid, aspartate transaminase, alanine transaminase, alanine phosphatase, lactate dehydrogenase, creatine kinase, lipids, total cholesterol, total bilirubin and glucose. For biodistribution, excretion and pharmacokinetics analyses, organs, fecal matter and blood were collected from mice euthanized at different time points post injection such as 4 h, 24 h, 48 h, 1 week and 2 weeks. The organs, fecal matter and blood samples were digested with nitric acid in a microwave digestion unit. The amount of NCs in the organs, excreta and in blood was analyzed with the help of ICP-MS. For *in vivo* anti-oxidant studies, liver samples collected post treatment were homogenized and the resultant supernatants were used for estimation of different antioxidant parameters such as LPO, GR, GPx, GSH and SOD. The amount of LPO was determined and expressed as nmol per mg protein. The GR activity was determined by measuring the reduction of GSSG in the presence of NADPH. The GR activity was expressed as units per mg protein. The level of GSH in the liver homogenate was

determined using DTNB (5,5'-dithiobis (2-nitrobenzoic acid)) and the amount of GSH was expressed as nmol per mg protein. The activity of GPx was then assayed by measuring remaining GSH after the enzyme-catalyzed reaction and the enzyme activity was expressed as units per mg protein. Superoxide dismutase was assayed using the modified pyrogallol method and the SOD was expressed in units per mg protein. Spleens obtained from control and treated groups were utilized to analyze the proliferative ability of splenocytes as well as spleen coefficient. The splenocytes were isolated, cultured and assayed for proliferation using alamar blue assay. Weights of the mice and spleen were measured post therapy to calculate the spleen coefficient. DNA was extracted from the brain samples collected from the control and treated mice using GenElute Mammalian DNA Isolation Kit (Sigma Aldrich) as per the manufacturer's instructions and the extracted DNA was used for 8-OHdG detection by a competitive immunosorbent assay using New 8-OHdG Check (Japan Institute of Control of Aging, Japan) as per the manufacturer's instructions. The values obtained for LPO, GR, GPx, GSH, SOD, splenocyte proliferation, spleen coefficient and 8-OHdG were cumulatively expressed in terms of fold increase in comparison to control. For x-ray contrast imaging studies, Balb/c mice were inoculated subcutaneously with MCF-7 cells at their forelimb flank. Post-subcutaneous implantation, the tumors were allowed to grow to a palpable mass. The subcutaneous tumor-bearing mice were injected intratumorally with the NCs at 5 adjacent locations (10 μ L of NCs at each site at a concentration of 1 mg/mL) so as to distribute the NCs as much as possible throughout the tumor and the mice were subsequently imaged using a μ CT instrument. For PDT experiments, four groups of mice were utilized: 1) controls, injected with saline without NIR laser irradiation; 2) injected with saline + NIR laser irradiation; 3) injected with NCs without NIR laser; and 4) NCs + NIR laser irradiation. The subcutaneous tumor-bearing mice were injected intratumorally with the saline/NCs at 5 different places (each injection 10 μ L of 1 mg/mL). The tumors in group 2 and 4 mice were irradiated with ultra-low laser power for 15 min for 5 consecutive days. After the treatment period, the mice were observed for a period of 15 days, during which the behavioral, feeding and weight aspects were monitored. Subsequently, the mice were intravenously injected with annexin *in vivo*, and were euthanized for tumor collection. The tumors were then arranged according to their groups and photo-documented. The volume (calculated by their length, breadth and depth measurements), weight

and annexin intensity of tumors were calculated. The tumors from the respective groups were then fixed and sectioned for routine H&E staining and the images were recorded with a brightfield microscope.

Statistical analysis

All quantitative experiments were conducted with at least three independent experiments. Data were analyzed by a one-way ANOVA for multiple data set analyses and were expressed as mean \pm SD. A difference was considered statistically significant when $p < 0.05$.

Results and Discussion

NC synthesis and characterization

Cu₃BiS₃ NCs were prepared by a conventional organometallic hot-injection method. The hot solvents aid in nucleation as well as capping of the NCs. The yield obtained per batch of synthesis was quite optimal (approximately 675 mg) and the ease of NCs synthesis is an advantage. The as-synthesized NCs were of relatively uniform size with polygonal/spherical shape and an average diameter of about 12 ± 4 nm as analyzed by transmission electron microscopy (TEM) (Figure 1A-C). Selected area electron diffraction (SAED) analysis confirmed the highly crystalline nature of the particles as observed with high resolution TEM (HR-TEM) (Figure 1A, inset). Elemental analysis exhibiting an approximate ratio of 3:1:3 for Cu, Bi and S respectively (Figure S1A) and scanning transmission electron microscopy (STEM) mapping confirmed the presence of Cu, Bi and S, distributed uniformly throughout the crystals (Figure 1E). The phase analysis of NCs was determined by x-ray diffraction (XRD). All peaks in the pattern correspond to reflections of the Wittichenite phase of Cu₃BiS₃ NCs, matching well with reported values (JCPDS Card No. 43-1479) (Figure 1D). The composition and valence states of Cu₃BiS₃ NCs were studied by x-ray photoelectron spectroscopy (XPS) (Figure 1F). The survey spectrum, Cu 2p, Bi 4f and S 2p core levels demonstrate the presence of Cu, Bi and S in sample. The doublet feature of Cu 2p spectrum due to spin orbit splitting result into 2p_{3/2} (931.8 eV) and 2p_{1/2} (951.8 eV) peaks with FWHM of 2.28 and 2.39 eV respectively and clear separation of peaks by 20 eV, suggesting that Cu ion exists in the Cu (I) state [12]. There is no 'shake-up' in the higher binding energy direction, which indicated the absence of Cu (II) and their oxides. The Bi 4f peaks split into Bi 4f_{5/2} (163.28 eV) and Bi 4f_{7/2} (157.5 eV) with FWHM of 2.06 and 1.48 eV respectively. The S 2p level was resolved into single spin orbit splitting: S 2p_{3/2} and S 2p_{1/2} with binding energy maxima at 162.00 eV and 162.70 eV respectively with a separation

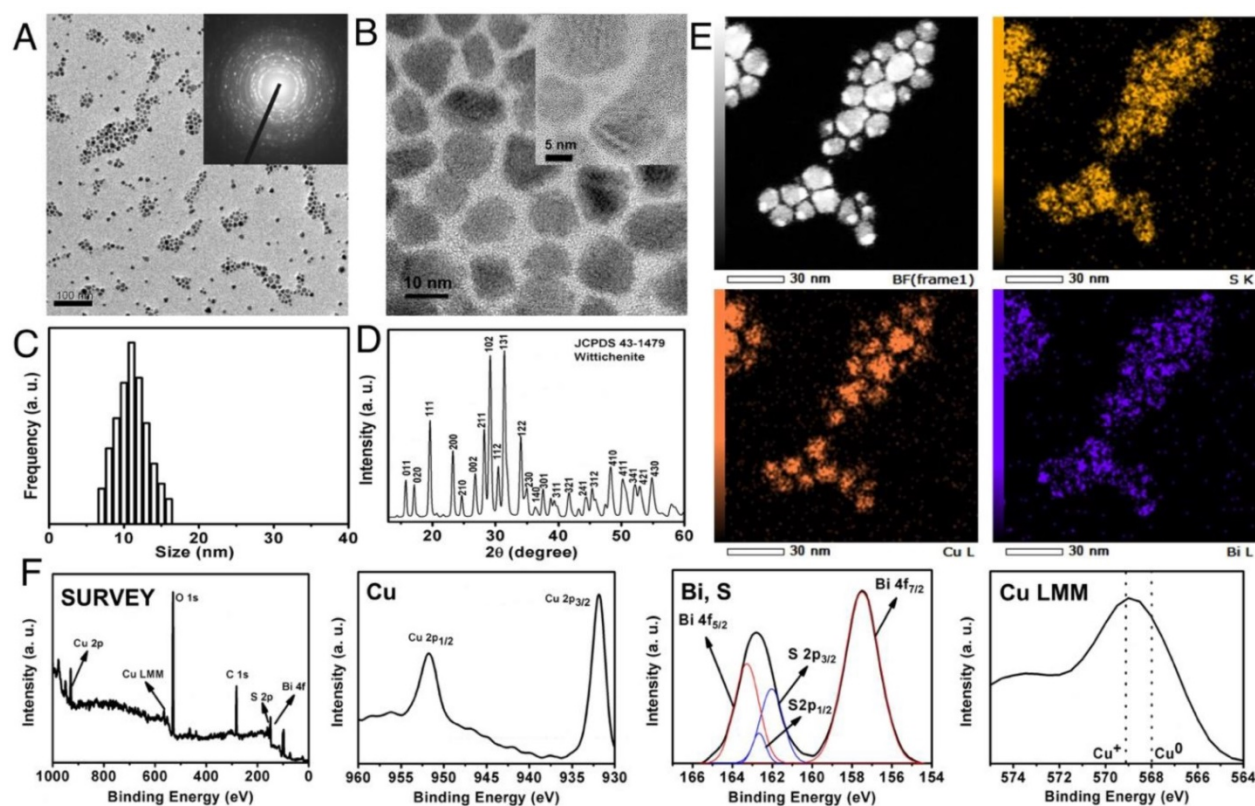


Figure 1. NC characterization. (A) Typical low and (B) high-resolution TEM images of Cu_3BiS_3 NCs. Inset (A) shows the SAED pattern of NCs confirming the crystalline nature of the NCs. Scale bar in (A) corresponds to 100 nm, (B) corresponds to 10 nm and the scale bar of inset in (B) corresponds to 5 nm. (C) Size profile of NCs analyzed by random counting of 200 NCs, depicting an average NC size of 12 ± 4 nm. (D) Powder XRD patterns of the as-prepared nanocrystals from JCPDS card No. 43-1479 confirming the Wittichenite crystallization pattern. (E) STEM-EDS elemental maps of the individual nanocrystals showing the presence of S, Cu and Bi. (F) XPS spectrum of the NCs exhibiting wide (survey) spectrum, Cu, Bi, S peaks, and the LMM state of Cu.

of 0.70 eV and the ratio intensity of the two components was 2:1. A peak maximum at 162 eV indicated metal sulfide and any peak beyond 165 eV denoted absence of oxidized sulfur. These observations clearly showed that the nanocrystalline metal sulfide formed were pure. When the NCs' optical properties were analyzed, a clear onset of absorption in the NIR region at 800-1100 nm was observed (Figure S1B). This might be due to the surface plasmon resonance generated by the minority hole carriers, which is a common feature of metal-deficient chalcogenide nanocrystals [14]. This clear absorption in the NIR region holds promise in potential applications such as photoacoustic imaging and/or phototherapy. The band gap of NCs was calculated by drawing a tangent towards the x-axis in the absorption squared versus energy graph and was found to be 1.88 eV (Figure S1B, inset).

PEGylation

To impart compatibility for biological applications, the Cu_3BiS_3 NCs were coated with lipid-PEG in a facile manner, which is also known to confer upon the NCs stability and monodispersity in aqueous solvents. FT-IR analysis of PEGylated NCs

exhibited signature peaks of lipid-PEG, indicating successful surface coating (Figure S2A). The lipid-PEGylated NCs were monodisperse in prominent biological media such as PBS and animal cell culture medium. Thus, the NCs were hydrophilic, implying that they can directly realize their bio-applications without complex surface modifications. The aqueous dispersion exhibited a black color and remained stable. The hydrodynamic diameter and zeta-potential of PEGylated NCs were found to be 150.2 nm and -36.6 mV respectively (Figure S2B-C). The zeta potential value indicated that the PEGylated NCs would be highly stable in physiological pH solutions. All biological experimentations were hence carried out employing the PEGylated Cu_3BiS_3 NCs.

NC uptake and cytocompatibility

The uptake efficiency of Cu_3BiS_3 NCs was investigated using ICP-MS on HMEC (normal mammary epithelial cells) and the breast adenocarcinoma MCF-7 cell line. The results reveal that the cellular uptake of NCs was observed to be dose dependent (Figure S3A) in both cell lines. It has to be noted that the ICP-MS analysis was performed

after thorough washing of the cells to remove un-internalized or free NCs, and the values obtained represent the internalized particles, providing proof of the efficient entry of NCs into the cells. With the entry of NCs confirmed, their cytocompatibility was assessed using alamar blue assay (**Figure S3B**), which is a pre-requisite when considering the NCs for cellular/*in vivo* applications. Cell viabilities of both MCF-7 and HMEC were not hindered with the treatment of NCs. At the highest dose tested, 1mg/mL, a slight decrease in viability was observed, though it stayed above 80% for both cell lines. The results suggest that NCs were generally compatible to the cells with relatively low to negligible level of toxicity. *In vitro* cytocompatibility studies revealed the non-toxic nature of NCs post-PEGylation (**Figure S3B**), which formed the basis for all future *in vitro* and *in vivo* assays.

***In vitro* and *in vivo* CT imaging**

MicroCT imaging is a widely used diagnostic method owing to its deep tissue penetration and high resolution. With a higher x-ray attenuation coefficient ($5.74 \text{ cm}^{-2} \text{ kg}^{-1}$), Bi is proposed to be a better contrast media than other conventional contrast elements such as Au ($5.16 \text{ cm}^{-2} \text{ kg}^{-1}$), W ($4.44 \text{ cm}^{-2} \text{ kg}^{-1}$), and I ($1.94 \text{ cm}^{-2} \text{ kg}^{-1}$) (all values at 100 keV) [36, 44]. Also, Bi chalcogenides exhibit better blood half-lives compared with small iodinated molecules [45]. A clear concentration-dependent contrast enhancement of NCs upon x-ray stimulation was observed (**Figure S4A**). The 3D z-stack reconstruction of an x-ray CT image of Cu_3BiS_3 NCs (0.25 mg/mL) on a Whatman filter paper-1 displayed noticeable signal enrichment (**Figure S4B**), demonstrating the prospective application of the NCs as μCT contrast agents. To assess whether similar contrast signals could be obtained from biological samples, MCF-7 cells, pre-incubated with Cu_3BiS_3 NCs at concentrations of 0.25 and 0.5 mg/mL were exposed to x-rays. Visibly, high-contrast signals were recorded in the Cu_3BiS_3 treated cells whereas the control cells devoid of NCs presented no contrast. These *in vitro* observations (**Figure S4A-B**) implied the role Cu_3BiS_3 NCs could play as high-contrast media in biological entities. To confirm this hypothesis, NCs were injected subcutaneously into MCF-7 xenograft tumors in mice and analyzed under x-ray irradiation. The corresponding injection sites at five different points exhibited a brighter contrast than other soft tissues (**Figure 2A-E** and **Video S1**). **Figure 2B** shows a particular slice of a mouse body with high signal intensity from Cu_3BiS_3 NCs and **Figure 2C** displays the whole-body 3D x-ray image where the presence of NCs could be clearly visualized in comparison to the

skeletal structure and further provide clear images of the enhanced contrast and location of NCs in tumor. In addition, thickness mapping of the contrast signal, or in other words the NC distribution pattern obtained via 3D construction of injected NCs, revealed an even distribution of NCs across the tumor volume (**Figure 2D-E**). The x-ray CT imaging capability demonstrates significant promise for PEGylated Cu_3BiS_3 NCs in bioimaging and cancer diagnosis.

***In vitro* photothermal therapy**

The advantages of photothermal therapy (PTT) are high selectivity, excellent efficacy, and minimal invasiveness compared to traditional clinical therapeutic methods. Their strong absorption in the NIR region makes it possible to use Cu_3BiS_3 as photothermal agents. To verify the potential of using them as PTT agents, NC solutions of varying concentrations (10, 25, 50, 100 and 200 ppm) were exposed to an 800 nm NIR laser (**Figure S5A-B**). The thermal effects of NCs were dose dependent, indicating that the temperature elevation was highly reliant on the concentration of NCs exposed to laser irradiation. These results confirmed that Cu_3BiS_3 could rapidly convert the 800 nm laser energy into heat, which could be efficiently harnessed to deal irreversible damage to desired cells. Subsequently, the photothermal conversion efficiency (PCE) of NCs was measured, which was calculated to be 19.8% (**Figure S5C-D**). Next, we evaluated the *in vitro* photothermal ablation capacity of Cu_3BiS_3 NCs (0.1 mg/mL) on MCF-7 cells. Post NIR laser irradiation (2 min) and staining with Calcein (live)/PPi (dead), the cells were imaged under a high-speed confocal laser scanning microscope (CLSM) in green (calcein-live) and red (PPi-dead) channels (**Figure S6A**). It was visibly evident that a demarcated zone of irradiation could be observed in the Cu_3BiS_3 NCs + NIR panel. The region of laser incidence was completely dead with no viable cells. No such observations were made with any other groups, where most cells exhibited bright calcein staining depicting their metabolically active nature. To quantitatively evaluate the *in vitro* cancer cell killing effect of Cu_3BiS_3 NCs with NIR irradiation, the viability of cells post PTT treatment was determined (**Figure S6C**), which was found to be 10%, correlating with the CLSM observations and confirming the high photothermal conversion ability of NCs leading to efficient cancer cell killing. Though the present work is focused on the low-power PDT ability of Cu_3BiS_3 NCs, the PTT effect further adds dimension to the multi-therapeutic potential of NCs.

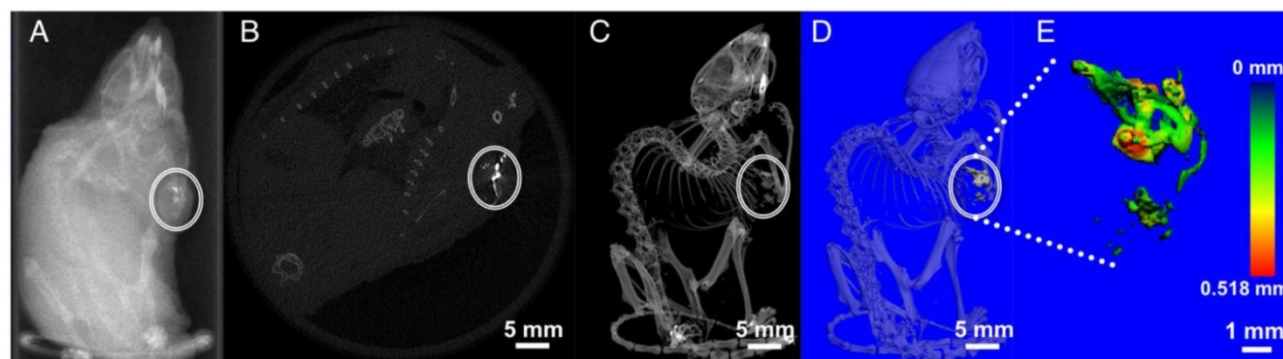


Figure 2. X-ray contrast imaging. (A) In vivo transverse section (scout view) imaging of a mouse following intratumoral injection of NCs. (B) Cross sectional slice exhibiting bright contrast due to NC distribution in the tumor region (circle). (C) X-ray image of the mouse body with distinct contrast from the NCs in the tumor. (D-E) 3-D reconstruction of NCs accumulation, portraying a wide area of distribution throughout the tumor mass.

In vitro PDT

Further, we evaluated the generation of ROS in MCF-7 cells exposed to Cu_3BiS_3 NCs with and without NIR laser irradiation. In this confocal microscope-based assay, Cell-ROX tracker (green) was used to assess intracellular ROS production from cells. **Figure S6B** shows that prominent fluorescence signals were found in approximately all the cells in the NCs-treated group upon irradiation with NIR laser when compared to control groups. Absence of any signal in the Cu_3BiS_3 NCs-treated group (devoid of NIR), underlines the role of NIR laser in the production of ROS and the inability of NCs to do so on their own. The ROS generated by activation of Cu_3BiS_3 by NIR laser can attack cellular macromolecules and cause severe deleterious and irreversible effects on cellular metabolic processes like growth and viability, resulting in effective PDT. To evaluate and compare the *in vitro* cancer cell killing effect of Cu_3BiS_3 NCs with and without NIR irradiation, the viability of MCF-7 cells post treatment was determined. The PDT-ROS mediated toxicity killed approximately 65% cells within 4 h post NIR irradiation (**Figure S6C**). Thus, Cu_3BiS_3 NCs show potential as a new class of photosensitizers allowing for cancer cell killing by PDT under extremely low-power NIR irradiation. *In vitro* experiments confirmed the NIR-mediated ROS generation (**Figure S6B-D**) and subsequent cell death (**Figure S6C**). NP-based PDT systems are a perfect solution to significantly improve the performance of therapy, especially NIR-responsive modules. We believe that the NIR sensitization of Cu_3BiS_3 NCs leads to ROS production via Cu ion leaching. NIR irradiation of Cu-based NCs in aqueous solution has been known to leach Cu ions, which enhances the generation of ROS. This effect is highly specific as it occurs only upon NIR irradiation [21]. The leached Cu ions are known to accelerate ROS production via Haber-Weiss and Fenton reactions [34]. The leached ions could get

reduced intracellularly by ascorbic acid or glutathione, and subsequently react with hydrogen peroxide to generate hydroxide and a hydroxyl radical. In addition, the NIR irradiation favors energy transfer from NCs directly to molecular oxygen. The band gap of Cu_3BiS_3 NCs is approximately 1.88 eV (**Figure S1B**, inset), which is higher than the energy band gap of singlet oxygen (0.97 eV) [28], thus facilitating energy transfer from the surface of the NCs to molecular oxygen upon NIR irradiation. This energy transfer further facilitates formation of singlet oxygen. The possible mechanism of ROS production upon NIR irradiation of Cu_3BiS_3 NCs is presented in **Figure 3A**. The physical sensitization and chemical resultants are displayed. The substantial ROS produced upon NIR irradiation of Cu_3BiS_3 NCs is generally short lived and can oxidize a wide array of macromolecules such as DNA and proteins, resulting in a high degree of cell damage. To establish that NIR irradiation can lead to leaching of Cu ions, we exposed the NC buffer solution to laser irradiation for 10 min. Control solution of NCs without NIR irradiation was also maintained. The supernatants of the respective solutions were collected by centrifugal force and were subjected to ICP-MS analysis to quantify any leached Cu ions. As expected, the irradiation batch exhibited 0.8% leached Cu ions compared to negligible Cu ions in control (0.001%), confirming the role of laser irradiation in facilitating Cu ion leaching. To affirm whether the leached Cu ions serve as the source of ROS, a fluorescence assay based on dichlorofluorescein diacetate (DCFH-DA) was performed [24]. Blank (water), 808 nm NIR-irradiated water and NC suspension without NIR exposure failed to generate ROS, and thus no fluorescence could be quantified (**Figure 3B**). However, the NC suspension exposed to NIR laser generated ROS in significant quantity and thus a clear emission of DCF was seen, reaffirming the role of NIR irradiation for the ROS phenomenon.

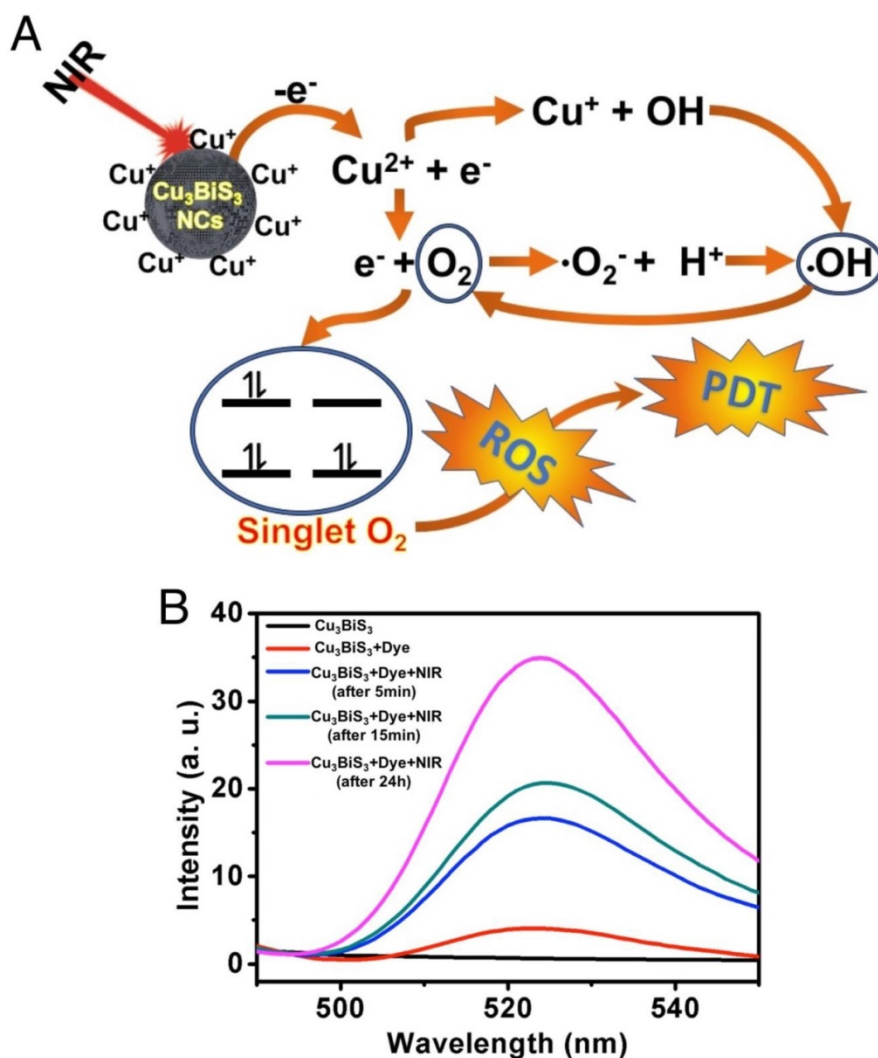


Figure 3. NIR-induced ROS generation. (A) Mechanism of reactive oxygen species generation from Cu_3BiS_3 NCs upon NIR laser irradiation. **(B)** Photoluminescence spectra of DCF, a ROS tracer, in aqueous suspension of NCs that were either exposed/unexposed to 808 nm NIR laser irradiation. The emission peak centered at 520 nm confirms the production of singlet oxygen upon irradiating the NCs with NIR laser.

In vivo PDT

PDT is known to treat lesions on or under the skin, or in solid organs that can be reached with the light source being employed. Therefore, penetration (skin/deep tissue) of the light source is a critical factor when considering PDT. For this reason, PDT is a well-known and preferred therapeutic modality for many skin-related disorders. Numerous reports address the use of PDT in superficial/sub-cutaneous skin cancers/diseases. To emulate the PDT-mediated cancer killing observed *in vitro*, under *in vivo* skin cancer/tumor mass-like conditions, sub-cutaneous MCF-7 tumor xenograft-bearing mice were injected intratumorally with Cu_3BiS_3 NCs or saline. Intratumoral injection mode was preferred over intravenous mode to avoid accumulation in other organs as the NCs were not functionalized with any cancer-targeting epitopes, which also provides the opportunity to maximize the intended therapeutic

outcome by focusing specifically on the region of interest with a minimal dose of NCs. Accordingly, intratumoral injections of Cu_3BiS_3 NCs were performed, distributed equally at five sites around the tumor, deviating from the conventional style of single point injection (Figure 4A, inset). The objective of adopting this injection style was to have as much of the NCs distributed in the whole of the tumor so as to maximize the area of effect on laser exposure. 10 min post injection, animals were anesthetized and the tumor region was irradiated with NIR laser for 15 min. The temperature changes were monitored periodically. As could be inferred from infrared thermal images, there was no rise in temperature upon irradiation of the saline- or NC-injected groups (Figure 4C). Respective temperature histograms of tumor regions (black circle) of saline- and NCs-injected mice under NIR irradiation depict no noticeable change from the pre-irradiation

histograms. As NCs in suspension have a black appearance, the skin (over the tumor) of the injected mice has a black tinge (**Figure 4A-B**); however, post laser exposure the tinge was more prominent (**Figure 4B**) and seemed to continue to darken post each exposure. This was not the case with control mice (**Figure 4A-B**), which retained their usual skin tone. NIR irradiation was carried out for 5 consecutive days, each treatment lasting for 15 min. After the 5-day treatment schedule, the mice were kept in animal housing conditions for a further period of 15 days to observe the behaviors of both tumors and mice. The mice were monitored with regards to their movement, feeding (solid food and water) and reflex response (to sudden touch), apart from tumor growth. All mice, regardless of observation group, displayed no abnormal behavioral characteristics. However, as days progressed, except the Cu_3BiS_3 +NIR group, all other groups had slight difficulty in walking and feeding (**Table S2**) as the food pellets and water source needed to be reached out to for access, though their level or alertness to touch was unchanged. Additional pain analysis was carried out based on published literature [46, 47]. When mice experience pain, they demonstrate abnormal behavior in terms of appetite (less food/water intake) and activity (reluctance to move, reduced grooming, hunch posture, increased aggressiveness or self-mutilation such as biting the pain site), etc. We keenly observed for these features pre-, during- and post-therapy. However, we did not find any abnormalities in the treated group (**Table S2**). We also checked the nesting behavior of each subject pre- and post-therapy; once again no abnormal features were observed, indicating that the treated mice subjects were pain free during and post-treatment. Body weights of control and treatment group mice measured pre- and post-treatment confirmed that mice in the Cu_3BiS_3 +NIR group exhibited optimal weight gain, whereas other groups exhibited a systemic decrease in weight (**Figure 5A**). With regards to tumor, visual observation along with external measurement revealed that control groups, saline/ Cu_3BiS_3 NCs injected without NIR exposure and saline with NIR exposure had a gradual increase in tumor size, which was probably the reason for their restricted movement and feeding behavior. The tumor was present on the right forelimb shoulder and hindered casual use of that limb. Reduced food/water intake was correlative with the weight loss observed in these groups (**Figure 5A**). After 15 days of observation, mice were injected with *in vivo* annexin that can trace and label dead cells in live animals. Mice were then euthanized and the tumors excised and used for further analysis. It was clearly evident from **Figure 5B** that tumors were

greatly curbed in the Cu_3BiS_3 +NIR group, whereas the rest had a larger and more obvious tumor mass. The Cu_3BiS_3 +NIR tumors appeared to be much drier and lighter when compared with those of other groups, possibly reflecting starvation of the tumor mass due to lack of nutrient/blood supply. A note of mention is that during excision, a number of blood vessels were seen surrounding the tumors of other groups whereas no such signs were present in the Cu_3BiS_3 +NIR group, prompting a speculative assumption that the Cu_3BiS_3 NCs-mediated PDT could invariably curb angiogenesis, new blood vessel formation, and deplete the existing ones as well. Also, the striking black color of the Cu_3BiS_3 +NIR tumors was visually apparent. Though this could be attributed to the black color of NCs, the NCs-injected group (devoid of NIR) did not exhibit the same appearance except for the presence of a few black spots/streaks. The most relevant explanation for the blackened appearance of the Cu_3BiS_3 +NIR tumors seems to be the considerable shrinkage of tumor mass, which must have concentrated the NCs, aided by the lack of circulation due to possible absence of blood vessels, resulting in extensive blackening. This observation is relative to the post-NIR laser exposure tinge seen on the skin over the tumor area (**Figure 4B**). During the excision, the skin covering the tumor was examined separately and the color tone was much lighter when compared to the darker tone observed with the tumor. After excision, it became evident that blackening of the tumor mass was affecting the visual appearance of the skin over it. It seems apt to mention at this point that the PDT performed using Cu_3BiS_3 NCs did not have skin altering/scaring properties and should be safe for such dermal/sub-dermal operations. As expected, and corresponding to the photographic evidence from **Figure 5B**, the tumor weight (**Figure 5C**) and volume (**Figure 5D**) of the Cu_3BiS_3 +NIR group were considerably reduced when compared with those of control (saline), control (saline)+NIR and NC groups, complementing the claim of starvation of tumors by arresting angiogenesis. It has to be noted that these observations were 15 days post-treatment, which implies that the Cu_3BiS_3 +NIR did extremely well in drastically curbing tumor growth and proliferation, even in the absence of continuous NIR exposure. Additional evidence for this statement can be seen from the annexin accumulation results (**Figure 5E-F**). Pronounced fluorescence was observed in the Cu_3BiS_3 +NIR group, whereas negligible to no fluorescence was observed in other groups, confirming that the leftover tumor cells were indeed dead (necrotic mass) with no further potential to multiply. Histology of tumors also confirmed that Cu_3BiS_3 +NIR tumor exhibited a necrotic tumor mass

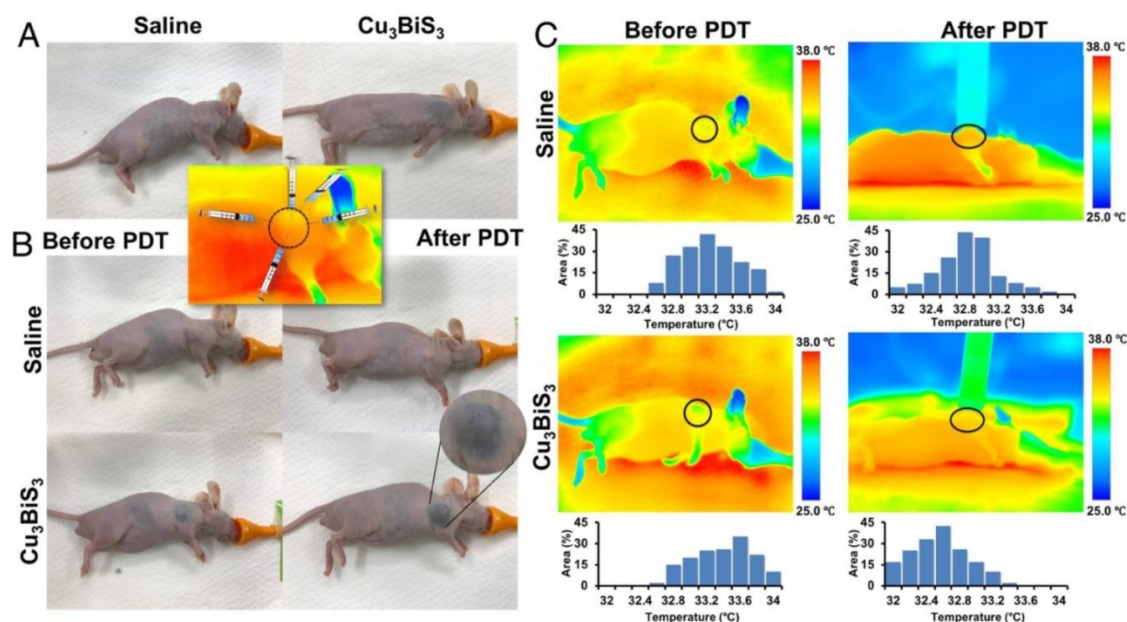


Figure 4. In vivo PDT. (A-B) Photo-documentation of mice in the control and treatment groups. (A) Control (saline) and Cu_3BiS_3 NCs-injected mice without any NIR exposure. The inset depicts the different NCs injection positions into the tumor. The tumor region is marked with a black circle. (B) Pre- and post-NIR laser exposure images of saline and Cu_3BiS_3 NCs groups, respectively. The highlighted region of the Cu_3BiS_3 NCs mouse shows the skin/tumor blackening upon laser exposure, but no signs of scar formation, therefore negating any heat-induced injury or charring. (C) Infrared thermograms of mice before and during (14 min into exposure) NIR irradiation are shown. The temperature profiles in the tumor regions denoted by the black circles are plotted in respective thermograms. There was no rise in temperature in both the saline and Cu_3BiS_3 NCs groups (both remained similar to the initial temperature at the start of the experiment) upon NIR laser irradiation, indicating the absence of generation of any heat.

with minimal to no viable cells (Figure 5G), whereas the saline, saline+NIR and NC groups exhibited viable tumor cells.

Copper, due to being a soft acid, is labile to physical and chemical stress. It has been shown previously that Cu-based NCs leach Cu ions upon acidic environment exposure or via physical irradiation [24]. We believe that similar observations were made in the present study leading to PDT. Though the NCs were PEG coated, upon irradiation the coating could become destabilized and lead to Cu ion leaching. In addition, the destabilized coating exposes the NCs to acidic tumor environment which can further lead to upregulated Cu leaching. This may be the reason for such prominent PDT effects with a low laser power. In addition, as shown in the UV-vis absorption data, the NCs exhibit good absorption around 800 nm. This can lead to efficient energy trapping that translates into elevated Cu ion leaching. Also, Bi has a higher extinction co-efficient that can help in capturing more photons in an efficient manner. This could also help in increasing reactivity and subsequent ROS production. Additionally, the larger Bi atom helps in scattering light with negligible photon loss through transmission, thus utilizing the energy towards PDT. We believe that the exceptional PDT effects at such low laser power are due to these cumulative properties of the Cu_3BiS_3 NCs. These results agree with our observations that singlet

oxygen is one of the ROS produced from NIR-activated NCs. The formation of singlet oxygen via Cu leaching or LSPR-based energy transfer from the NCs in acidic environment upon activation by near-infrared light confirms the ability of NCs to sensitize cancer masses effectively for better therapy.

In vivo biodistribution and biocompatibility

With the application-oriented investigations completed, further tests of the biocompatibility of Cu_3BiS_3 NCs in mice to ascertain their safety/toxicity profile were performed. Mice that were acclimatized in optimal animal housing conditions were divided into two major groups: controls that were injected intravenously with saline, and test group that were injected with Cu_3BiS_3 NCs. Weight profiles of mice were recorded until week 2. There were no significant variations in the weight of mice during the observation period (Figure 6A), with both control and test groups gaining weight on par with each other, suggesting a preliminary safety profile for the Cu_3BiS_3 NCs. Mice were euthanized at 4 h, 24 h, 48 h, 1 wk and 2 wk time points and the organs, fecal matter and blood collected for various analyses. The biodistribution of particles in major organs was examined at 4 h, 24 h, 1 wk and 2 wk using ICP-MS. Major organs such as brain, heart, liver, spleen, lung, kidney and blood were analyzed for presence of Cu and Bi (Figure 6B-C), respectively. Most of the injected particles after 4 h were seen to be in

circulation, confirming their prolonged blood half-life by escaping mononuclear phagocyte system (MPS) capture. At 4 h, the NCs mostly accumulated in the liver and spleen, whereas few were detected in the lungs and kidneys. Brain and heart did not exhibit any significant NC accumulation at any point of study. The particle count decreased in all organs and blood with progression of time, most probably due to excretion. By 2 weeks, most of the NCs were expelled out from the system, depicting their non-accumulative behavior and the results were complemented by excretion profiling (Figure 6D). The pharmacokinetics of the NCs post injection exhibited a C_{max} of 0.82 ± 0.05 mg, T_{max} of 5 ± 3 min, and $T_{1/2}$ (half-life) of 360 ± 30 min. There were no indications of tissue damage or other anomalies in the major organs 1 and 14 days after administration (Figure 6F). Serum biochemistry 1 and 14 days post intravenous administration of NCs (Table S3), revealed insignificant physiological/biochemical differences between the experimental and control groups, except for an initial slight increase in lactate dehydrogenase (LDH) levels. However, post 14 days, the LDH level decreased considerably and remained comparable to that of the control group. Liver samples of control and test mice (1 and 2 weeks post treatment) were subjected to *in vivo* antioxidant defense mechanism analysis based on the concentrations of LPO, GSH, GR, GPx and SOD. Changes in the levels of these critical parameters were relatively similar in all the groups without any significant variations (Figure 5E). It was clear from these results that the NCs do not induce ROS, and thus do not interfere with anti-oxidant mechanisms. Next, we investigated the effects (if any) of NCs on spleen, which represents the cell-mediated immune function. The spleen co-efficient and splenocyte proliferation post treatment were measured. It was noted that both the spleen co-efficient and splenocyte proliferation were not affected by the NC exposure and remained comparable to those of controls, indicating that there is no immunogenic response triggered due to NC exposure. Further, to understand whether the exposure of NCs would induce any genotoxicity, we analyzed the 8-OHdG concentrations in brain samples of control and treatment group mice. There were no considerable alterations in the levels of 8-OHdG between the treatment and control groups, indicating that the induction of DNA adducts (8-OHdG) was comparable with the control values. Again, this assay assured that the NCs were highly biocompatible without any genotoxic effects. Hence, we surmise and conclude that the NCs are safe, compatible nano-bio-probes for diagnostic and therapeutic applications.

Conclusion

Providing newer and advanced treatment options, with none to minimal side effects, is the ultimate goal of any research. In this work, we fabricated Cu and Bi chalcogenide-based Cu_3BiS_3 NCs for use as a multipurpose cancer theranostic system with capabilities in x-ray contrast imaging and photo-dynamic/-thermal therapy. As revealed by optical measurements, the NCs can harvest a wide spectrum of NIR light, benefiting both local hyperthermia and ROS generation upon NIR laser irradiation. Studies of their *in vivo* antitumor effect performed in tumor-bearing mice clearly illustrated their success in inhibiting solid tumors using NC-mediated PDT under ultra-low NIR laser power, through the induction of tumor necrosis and apoptosis. The starvation of tumors, most conceivably through the curbing of blood vessels supplying nutrients, assures the complete arrest on future proliferation and relapse of the malignant mass. Also, the results obtained warrant the use of Cu_3BiS_3 NCs in a variety of skin-related pathologies such as actinic keratoses, basal cell carcinomas, intraepidermal squamous carcinoma, kaposi sarcoma, psoriasis, viral warts etc. In addition, PDT with such a low sensitizer dosage and laser power is cheap, easy to employ, expected to result in no long-term side effects, and permits less invasive treatment options, repeated treatments, short treatment times, no scarring/pain, and is an outpatient therapy. With use of NIR lasers, which have the ability to penetrate deeper through tissue, PDT therapy can be extended for use in certain deep-tissue cancers of the esophagus and bronchi as well. The strong CT imaging potential of the NCs could translate in realization of future imaging-guided therapeutic modules. The enticing prospect of utilizing a safe nanomaterial such as Cu_3BiS_3 with a portable low-power laser source is sure to bring the realization of an easy, scar-less, pain and side effects-free, reliable and reasonable treatment option sooner than expected. Though the utilization of such low power laser raises the questions of unwanted and spontaneous reaction of Cu_3BiS_3 NCs to normal light as well, the justification can be found in the fact that the test mice were not given any special care or caging and were maintained in normal light/dark regimes, which did not elicit any inadvertent response in the Cu_3BiS_3 NCs (without NIR) group. Therefore, it is safe to conclude that the NCs-mediated PDT could occur only upon highly focused NIR laser exposure. Also, as the NCs were highly responsive to a compact and portable NIR laser device (used in this work), the ease of use warrants the possibility that patients themselves might in the near future use this system (for specific kinds of

skin/subcutaneous issues) at their place and time of convenience, without the hassle of travelling to specialist hospitals and clinics every time, saving time, resources and energy.

Abbreviations

ANSI: American National Standards Institute; ATCC: American type culture collection; CLSM: high-speed confocal laser-scanning microscope; DCFH-DA: 2',7'-dichlorodihydrofluorescein diacetate; DSPE-PEG (2000) amine: 1,2-distearoyl-sn-glycero-3-phosphoethanolamine-N-[amino(polyethylene glycol)-2000] (ammonium salt); DTNB: 5,5'-dithiobis (2-nitrobenzoic acid); DMEM: dulbecco's modified eagle medium; EDS: energy-dispersive x-ray spectroscopy; FBS: fetal bovine serum; FWHM: full width at half maximum; GSH: glutathione; GSSG: glutathione disulfide; GPx: glutathione peroxidase; GR: glutathione reductase; H&E: hematoxylin &

eosin; HMEC: human mammary epithelial cells; 8-OHdG: 8-hydroxy-2'-deoxyguanosine; ICG: indocyanine green; ICP-MS: inductive coupled plasma-mass spectrometry; JCPDS: Joint Committee on Powder Diffraction Standards; LDH: lactate dehydrogenase; LPO: lipid peroxidation; LSPR: localized surface plasmon resonance; MPE: maximum permissible exposure; μ CT: micro computed tomography; NCs: nanocrystals; NPs: nanoparticles; NIR: near infrared; NADPH: nicotinamide adenine dinucleotide phosphate; PBS: phosphate buffered saline; PDT: photodynamic therapy; PTT: photothermal therapy; PCE: photothermal conversion efficiency; PPI: propidium iodide; ROS: reactive oxygen species; STEM: scanning transmission electron microscope; SAED: selected area electron diffraction; SOD: superoxide dismutase; TEM: transmission electron microscope; XRD: x-ray diffraction; XPS: x-ray photoelectron spectroscopy.

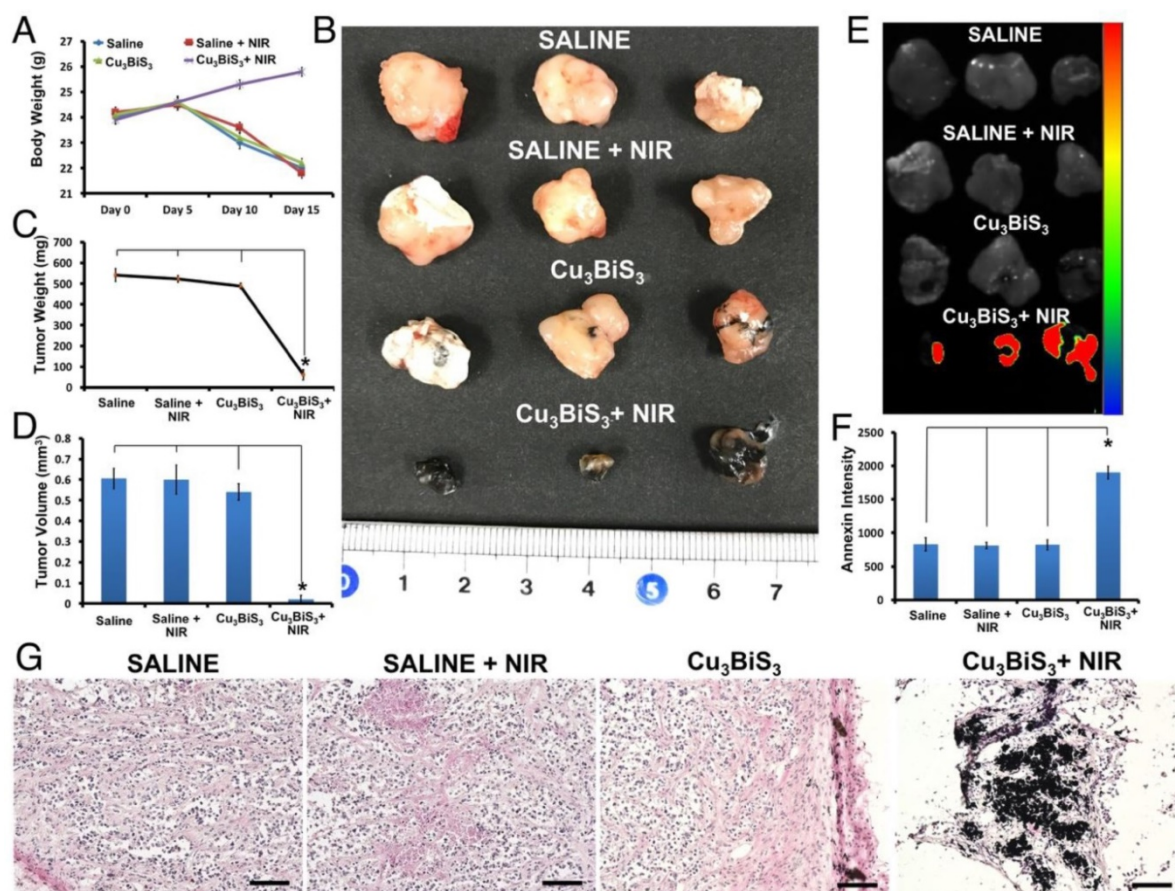


Figure 5. Therapeutic outcome. (A) Body weight of mice in control and treatment groups at different time points, with clear loss of weight in all groups except Cu₃BiS₃+NIR. (B) Representative tumor images 15 days post 5-day treatment period, indicating significantly shrunk tumors in the NC+NIR group. (C-D) Quantitative measurement of tumor weight and volume after treatment depicting the efficiency of NC-mediated PDT to drastically restrict tumor growth by a factor of 20 from the other groups. (E) In vivo annexin accumulation in the Cu₃BiS₃+NIR group confirms the dead and non-proliferative nature of the tumor mass. Lack of any such annexin-positive signals in the other groups is evidence of their live and active state of proliferation. (F) Quantitative measurement of annexin intensity in tumors after treatment was correlative of the visual observations in (E) with high signal intensity in the Cu₃BiS₃+NIR group. (G) H&E staining of sections collected from tumors of different groups of mice 15 days post 5 days of treatment showing the presence of viable tumor cells in all groups except the Cu₃BiS₃+NIR group, which exhibited a destructed tumor mass with black islands of accumulated NCs. Scale bar (G) represent 100 μ m. The data are represented as mean \pm SD. A difference was considered statistically significant when $p < 0.05$, indicated by *.

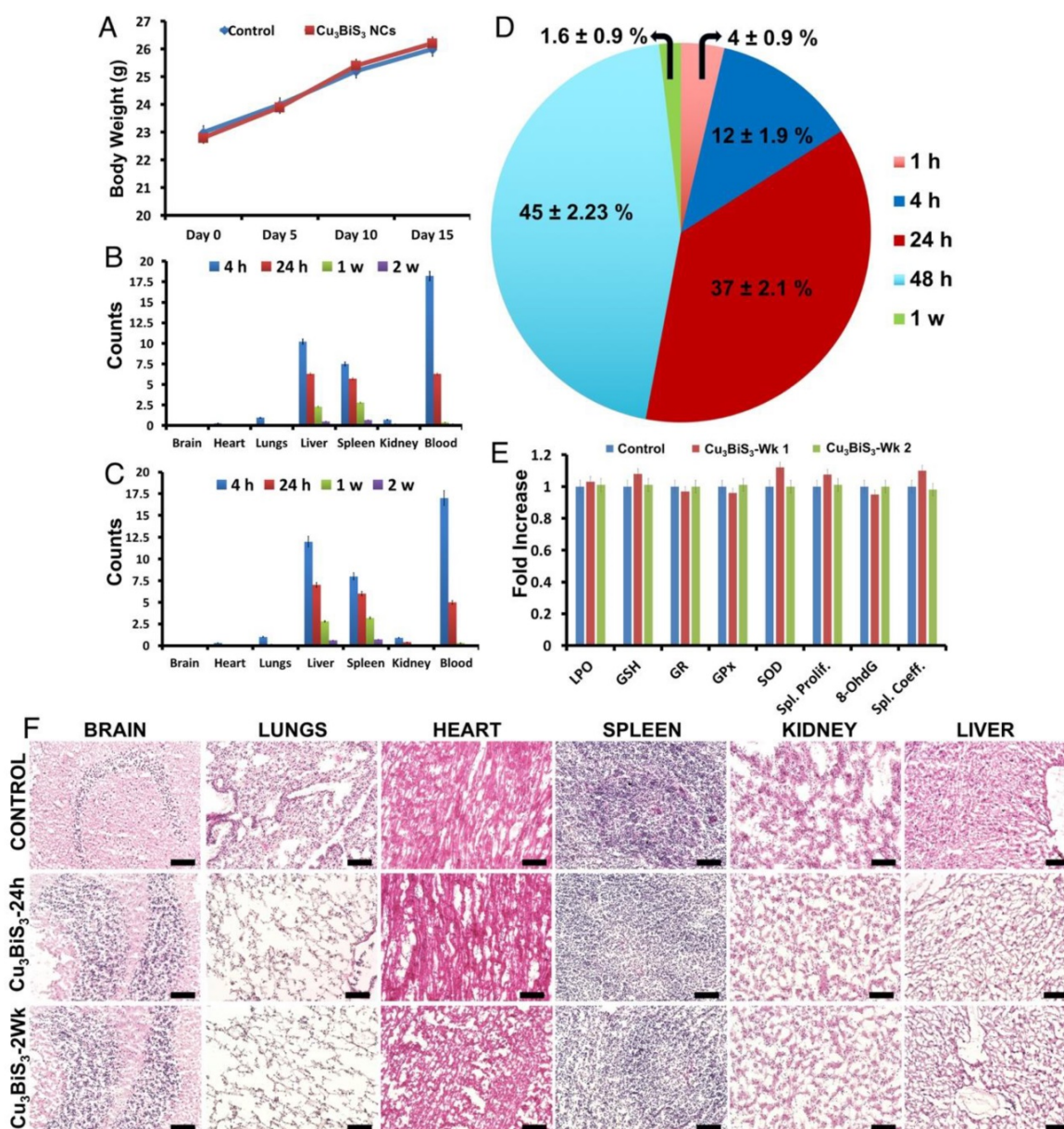


Figure 6. *In vivo* biocompatibility. (A) Body weight profile of control and treated mice that were intravenously injected with saline and NCs respectively, depicting a steady weight gain in both cases. (B–C) Biodistribution pattern of Cu and Bi, respectively, as obtained from ICP-MS analysis, post intravenous administration of NCs recorded at 4 h, 24 h, 1 week and 2 weeks. Initial maximum accumulation was observed in liver and spleen, with a still larger concentration in blood, highlighting the extended blood-circulation life of the NCs. (D) By 2 weeks, the NCs were completely cleared from the system. (E) Anti-oxidant, spleen proliferation, spleen co-efficient and brain 8-OHdG level measurements post systemic toxicity analysis, revealing the safety profile of Cu_3BiS_3 NCs. (F) H&E-stained histology sections of major organs collected from control as well as NC-treated mice. The administration of Cu_3BiS_3 NCs did not alter the histo-architecture, with no signs of inflammation visible even after 24 h and 2 weeks. Scale bar (F), represent 100 μm .

Acknowledgements

The authors would like to thank Prof. Susumu Ohshima, Biomedical Research Center, Division of Morphological Science, Saitama Medical University for providing access to microscope facilities in his lab. The authors would like to thank Ms. Yuko Suzuki, Biomedical Research Centre, Division of Analytical Science, Saitama Medical University, for preparation of reagents and consumables for *in vivo* experiments.

Supplementary Material

Supplementary figures and tables.

<http://www.thno.org/v08p5231s1.pdf>

Competing Interests

The authors have declared that no competing interest exists.

References

- Ogilby PR. Singlet oxygen: there is indeed something new under the sun. *Chem Soc Rev.* 2010; 39: 3181-209.

2. He C, Duan X, Guo N, Chan C, Poon C, Weichselbaum RR, Lin W. Core-shell nanoscale coordination polymers combine chemotherapy and photodynamic therapy to potentiate checkpoint blockade cancer immunotherapy. *Nat Commun.* 2016; 7: 12499.
3. Vankayala R, Sagadevan A, Vijayaraghavan P, Kuo CL, Hwang KC. Metal nanoparticles sensitize the formation of singlet oxygen. *Angew Chem Int Ed.* 2011; 50: 10640-10644.
4. Vijayaraghavan P, Liu CH, Vankayala R, Chiang CS, Hwang KC. Designing multi-branched gold nanoechinus for NIR light activated dual modal photodynamic and photothermal therapy in the second biological window. *Adv Mater.* 2014; 26: 6689-95.
5. Azzouzi AR, Lebdai S, Benzaghof F, Stief C. Vascular-targeted photodynamic therapy with TOOKAD soluble in localized prostate cancer: standardization of the procedure. *World J Urol.* 2015; 33: 937-44.
6. Jing T, Fu L, Liu L, Yan L. A reduction-responsive polypeptide nanogel encapsulating NIR photosensitizer for imaging guided photodynamic therapy. *Polym Chem.* 2016; 7: 951-7.
7. Ruan Z, Liu L, Jiang W, Li S, Wang Y, Yan L. NIR imaging-guided combined photodynamic therapy and chemotherapy by a pH-responsive amphiphilic polypeptide prodrug. *Biomater.* 2017; 5: 313-21.
8. Nioka S, Chance B. NIR spectroscopic detection of breast cancer. *Technol Cancer Res Treat.* 2005; 4: 497-512.
9. Feng F, Yue Y, Fei Z, Meng G, Tianmeng S, Jiaxin L, Zhang H, Qian H, Tao W, Yang X. Design of tumor acidity-responsive sheddable nanoparticles for fluorescence/magnetic resonance imaging-guided photodynamic therapy. *Theranostics.* 2017; 7: 1290-302.
10. Kievit FM, Zhang M. Cancer nanotheranostics: improving imaging and therapy by targeted delivery across biological barriers. *Adv Mater.* 2011; 23: H217-47.
11. Barreto JA, Malley WO, Kubeil M, Graham B, Stephan H, Spiccia L. Nanomaterials: applications in cancer imaging and therapy. *Adv Mater.* 2011; 23: H18-40.
12. Rong PF, Yang K, Srivastan A, Kiesewetter DO, Yue XY, Wang F, Nie L, Bhirde A, Wang Z, Liu Z, Niu G, Wang W, Chen X. Photosensitizer loaded nano-graphene for multimodality imaging guided tumor photodynamic therapy. *Theranostics.* 2014; 4: 229-39.
13. Ji T, Zhao Y, Ding Y, Nie G. Using functional nanomaterials to target and regulate the tumor microenvironment: diagnostic and therapeutic applications. *Adv Mater.* 2013; 25: 3508-25.
14. Cheon J, Lee JH. Synergistically integrated nanoparticles as multimodal probes for nanobiotechnology. *Acc Chem Res.* 2008; 41: 1630-40.
15. Gao J, Gu H, Xu B. Multifunctional magnetic nanoparticles: design, synthesis, and biomedical applications. *Acc Chem Res.* 2009; 42: 1097-107.
16. Poulouse AC, Veeranarayanan S, Mohamed MS, Aburto RA, Mitcham T, Bouchard RR, Ajayan PM, Sakamoto Y, Maekawa T, Kumar DS. Multifunctional Cu₂Te nanocubes mediated combination therapy for multi-drug resistant MDA MB 453. *Sci Rep.* 2016; 6: 35961.
17. Poulouse AC, Veeranarayanan S, Mohamed MS, Nagaoka Y, Aburto RA, Mitcham T, Ajayan PM, Bouchard RR, Sakamoto Y, Yoshida Y, Maekawa T, Kumar DS. Multi-stimuli responsive Cu₂S nanocrystals as trimodal imaging and synergistic chemo-photothermal therapy agents. *Nanoscale.* 2015; 7: 8378-88.
18. Mohamed MS, Poulouse AC, Veeranarayanan S, Aburto RA, Mitcham T, Suzuki Y, Sakamoto Y, Ajayan PM, Bouchard RR, Yoshida Y, Maekawa T, Kumar DS. Plasmonic fluorescent CdSe/Cu₂S hybrid nanocrystals for multichannel imaging and cancer directed photo-thermal therapy. *Nanoscale.* 2016; 8: 7876-88.
19. Jang B, Choi Y. Photosensitizer-conjugated gold nanorods for enzyme-activatable fluorescence imaging and photodynamic therapy. *Theranostics.* 2012; 2: 190-7.
20. Yue CX, Zhang CL, Alfranca G, Yang Y, Jiang XQ, Yang Y, Pan F, de la Fuente JM, Cui D. Near-infrared light triggered ROS-activated theranostic platform based on Ce₆-CPT-UCNPs for simultaneous fluorescence imaging and chemo-photodynamic combined therapy. *Theranostics.* 2016; 6: 456-69.
21. Vankayala R, Kuo CL, Sagadevan A, Chen P-H, Chiang C-H, Hwang KC. Morphology dependent photosensitization and formation of singlet oxygen (¹Δg) by gold and silver nanoparticles and its application in cancer treatment. *J Mater Chem B.* 2013; 1: 4379-87.
22. DeKosa MC, Crutchley R. Photosensitized singlet oxygen and its applications. *J Coord Chem Rev.* 2002; 233 (234): 351-71.
23. Kendall CA, Morton CA. Photodynamic therapy for the treatment of skin disease. *Technol. Cancer Res Treat.* 2003; 2: 283-8.
24. Tao AR, Sinersuksakul P, Yang PD. Polyhedral silver nanocrystals with distinct scattering signatures. *Angew Chem Int Ed.* 2006; 45: 4597-601.
25. Vankayala R, Kuo C-L, Nuthalapati K, Chiang C-H, Hwang K. C. Nucleus-targeting gold nanoclusters for simultaneous in vivo fluorescence imaging, gene delivery, and NIR-light activated photodynamic therapy. *Adv Funct Mater.* 2015; 25: 5934-45.
26. Otake E, Sakuma S, Torii K, Maeda A, Ohi H, Yano S, Morita A. Effect and mechanism of a new photodynamic therapy with glycoconjugated fullerene. *Photochem Photobiol.* 2010; 86: 1356-63.
27. Wang S, Riedinger A, Li H, Fu C, Liu H, Li L, Liu T, Tan L, Barthel MJ, Pugliese G, Donato FD, Dabbusco MS, Meng X, Manna L, Meng H, Pellegrino T. Plasmonic copper sulfide nanocrystals exhibiting near-infrared photothermal and photodynamic therapeutic effects. *ACS Nano.* 2015; 9: 1788-800.
28. Guo W, Guo C, Zheng N, Sun T, Liu S. Cs₂WO₆ nanorods coated with polyelectrolyte multilayers as a multifunctional nanomaterial for bimodal imaging-guided photothermal/photodynamic cancer treatment. *Adv Mater.* 2017; 29: 1604157.
29. Vankayala R, Huang Y-K, Kalluru P, Chiang C-S, Hwang KC. First demonstration of gold nanorods-mediated photodynamic therapeutic destruction of tumors via near infra-red light activation. *Small.* 2014; 10: 1612-22.
30. Guo W, Qiu Z, Guo C, Ding D, Wang TLF, Sun J, Zheng N, Liu S. Multifunctional theranostic agent of Cu₂(OH)PO₄ quantum dots for photoacoustic image-guided photothermal/photodynamic combination cancer therapy. *ACS Appl Mater Interfaces.* 2017; 9: 9348-58.
31. Kalluru P, Vankayala R, Chiang C-S, Hwang K. C. Photosensitization of singlet oxygen and in vivo photodynamic therapeutic effects mediated by pegylated W₁₈O₄₉ nanowires. *Angew Chem Int Ed.* 2013; 52: 12332-6.
32. Vankayala R, Lin CC, Kalluru P, Chiang CS, Hwang KC. Gold nanoshells-mediated bimodal photodynamic and photothermal cancer treatment using ultra-low doses of near infra-red light. *Biomaterials.* 2014; 35: 5527-38.
33. Xu J, Yang P, Sun M, Bi H, Liu B, Yang D, Gai S, He F, Lin J. Highly emissive dye-sensitized upconversion nanostructure for dual-photosensitizer photodynamic therapy and bioimaging. *ACS Nano.* 2017; 11: 4133-44.
34. Qiu K, Wang J, Song C, Wang LL, Zhu H, Huang H, Huang J, Wang H, Ji L-N, Chao H. Crossfire for two-photon photodynamic therapy with fluorinated ruthenium (ii) photosensitizers. *ACS Appl Mater Interfaces.* 2017; 9: 18482-92.
35. [Internet] ANSI Z136 standards. <https://www.lia.org/resources/laser-safety-information/laser-safety-standards/ansi-z136-standards>
36. Li J, Jiang F, Yang B, Song X. R, Liu Y, Yang H-H, Cao D-R, Shi W-R, Chen G-N. Topological insulator bismuth selenide as a theranostic platform for simultaneous cancer imaging and therapy. *Sci Rep.* 2013; 3: 1998.
37. Li L, Rashidi LH, Yao M, Ma L, Chen L, Zhang J, Zhang Y, Chen W. CuS nanoagents for photodynamic and photothermal therapies: Phenomena and possible mechanisms. *Photodiagnosis Photodyn Ther.* 2017; 19: 5-14.
38. Zhou SM, Ma D-K, Zhang S-H, Wang W, Chan W, Huang S-M, Yu K. PEGylated Cu₃BiS₃ hollow nanospheres as a new photothermal agent for 980 nm-laser-driven photothermochemotherapy and a contrast agent for x-ray computed tomography imaging. *Nanoscale.* 2016; 8: 1374-82.
39. Li A, Li X, Yu X, Li W, Zhao R, An X, Cui D, Chen X, Li W. Synergistic thermoradiotherapy based on PEGylated Cu₃BiS₃ ternary semiconductor nanorods with strong absorption in the second near-infrared window. *Biomaterials.* 2017; 112: 164-75.
40. Li B, Ye K, Zhang Y, Qin J, Zou R, Xu K, Huang X, Xiao Z, Zhang W, Lu X, Hu J. Photothermal theragnosis synergistic therapy based on bimetal sulphide nanocrystals rather than nanocomposites. *Adv Mater.* 2015; 27: 1339-45.
41. Yang Y, Wu H, Shi B, Guo L, Zhang Y, An X, Zhang H, Yang S. Hydrophilic Cu₃BiS₃ nanoparticles for computed tomography imaging and photothermal therapy. *Part Part Sys Charact.* 2015; 32: 668-79.
42. Liu J, Wang P, Zhang X, Wang L, Wang D, Gu Z, Tang J, Guo M, Cao M, Zhou H, Liu Y, Chen C. Rapid degradation and high renal clearance of Cu₃BiS₃ nanodots for efficient cancer diagnosis and photothermal therapy in vivo. *ACS Nano.* 2016; 10: 4587.
43. Yu G, Liu A, Jin H, Chen Y, Yin D, Huo R, Wang S, Wang J. Urchin shaped Bi₂S₃/Cu₂S/Cu₃BiS₃ composites with enhanced photothermal and CT imaging performance. *J Phys Chem C.* 2018; 122: 3794.
44. Zhou Z, Kong B, Yu C, Shi X, Wang M, Liu W, Sun Y, Zhang, Y, Yang, H, Yang S. Tungsten oxide nanorods: an efficient nanopatform for tumor CT imaging and photothermal therapy. *Sci Rep.* 2014; 4: 3653.
45. Liu YL, Ai KL, Lu LH. Nanoparticulate x-ray computed tomography contrast agents: from design validation to in vivo applications. *Acc Chem Res.* 2012; 45: 1817-27.
46. Kohn DF, Martin TE, Foley PL, Morris TH, Swindle MM, Vogler GA, Wixson SK. Public statement: guidelines for the assessment and management of pain in rodents and rabbits. *J Am Assoc Lab Anim Sci.* 2007; 46: 97-108.
47. Gaskill BN, Karas AZ, Garner JP, Pritchett-Corning KR. Nest building as an indicator of health and welfare in laboratory mice. *J Vis Exp.* 2013; 82: 51012. doi: 10.3791/51012.